ADVANCED FUNCTIONAL MATERIALS
www.afm-journal.de

Growth of Large Crystalline Grains of Vanadyl-Phthalocyanine without Epitaxy on Graphene

Alexander J. Marsden, Luke A. Rochford, Dawn Wood, Alexandra J. Ramadan, Zachary P. L. Laker, Tim S. Jones, and Neil R. Wilson**

The performance of organic semiconductor thin films in electronic devices is related to their crystal structure and morphology, with charge transport mobility dependent on the degree of crystallinity and on the crystallographic orientation. Here organic molecular beam deposition of vanadyl phthalocyanine is studied on graphene and it is shown that crystalline grains up to several micrometers across can be formed at substrate temperatures of 155 °C, compared to room temperature grain sizes of ≈30 nm. Transmission electron microscopy confirms the presence of long range order at elevated substrate temperatures and reveals that the molecules are stacked in an edge-on orientation, but are not epitaxially aligned to the graphene. The crystalline grain sizes are significantly larger on graphene than on disordered substrates such as graphene oxide and silicon oxide. The effect on charge transport is probed by conducting atomic force microscopy, with the high temperature films on graphene showing increased mobility and uniformity and decreased trap density. These results illustrate an important advantage for the integration of graphene electrodes with organic semiconductor devices: the homogeneous surface of graphene results in high diffusion and low nucleation rates for thin film growth, encouraging the formation of highly crystalline films even with nonepitaxial growth.

1. Introduction

Organic electronic devices are intensively studied as a way of reducing the cost, both financial and environmental, of the vast electronics industry.[1–5] Organic semiconductors (OSCs) have been used as the active layers in organic photovoltaics (OPVs)[6] and as the source-drain channel in organic thin film transistors (OTFTs).[3] While these devices show promise for replacing their inorganic counterparts, performance optimization is needed.

Performance improvements can come from adjusting the structure of the OSC molecules in the active layer: both the crystallography and the morphology of the OSC have a direct impact on the charge transport mobility.[7] For example, single crystals of organic molecules generally exhibit higher mobilities than polycrystalline films, which suffer from charge scattering from grain boundaries and charge trapping.[8,9]

The structure of OSC films is dependent on the method of deposition, the deposition conditions, and the interactions between the substrate and OSC. Here we focus on organic molecular beam deposition (OMBD),[10] where the OSC is sublimed in ultrahigh vacuum (UHV) forming a molecular beam which condenses directly onto the growth substrate. OMBD has several advantages for studying OSC thin film formation: the rate of deposition and thickness of film can be controlled, sequential deposition can be used to build complex heterostructures, and control of the substrate temperature can be used to gain further control over the OSC film morphology.[11,12] OMBD is appropriate for small molecule OSCs, such as the metallophthalocyanines (MPcs)[13] which have been widely studied as active materials in OTFTs[12] and OPVs.[6,14] Thin film morphology depends on the MPc used: some such as copper phthalocyanine (CuPc) are planar molecules, whilst others such as vanadyl phthalocyanine (VOPc) are nonplanar due to the oxygen atom projecting out of the ligand plane. While much work has been done on the planar phthalocyanines,[15–17] less attention has been paid to the nonplanar type,[18] despite their promising optical absorption profiles and high performance in OPVs[19] and OTFTs.[20] VOPc is studied here as an archetype for these nonplanar phthalocyanines.

There is considerable interest in understanding and controlling the crystallinity of MPc thin films, and increasing the substrate temperature during OMBD can lead to more crystalline films.[21] However, morphology and crystallinity are also substrate dependent; for example, templating layers such as CuI[11]

Dr. A. J. Marsden, Z. P. L. Laker, Dr. N. R. Wilson
Department of Physics
University of Warwick
Coventry CV4 7L, UK
E-mail: a.marsden@warwick.ac.uk;
neil.wilson@warwick.ac.uk
Dr. L. Rochford, D. Wood, Prof. T. S. Jones
Department of Chemistry
University of Warwick
Coventry CV4 7L, UK
A. J. Ramadan
Department of Materials
Imperial College London
South Kensington SW7 2BP, UK

DOI: 10.1002/adfm.201503594

or para-sexiphenyl (p-6P)[22] have both been used to structurally modify MPc films. For VOPc, elevated substrate temperatures have been used for morphological control when depositing onto CuI,[11] silicon oxide,[23] and p-6P on silicon oxide,[21] and when codeposited with C60 onto a C60 layer.[14]

Graphene is an attractive electrode for organic electronics due to its strength, flexibility, and conductivity.[24] Moreover, graphene is highly transparent, ideal for transparent conducting electrodes in OPVs,[25] and organic light emitting diodes (OLEDs).[26] In addition, graphene has been demonstrated as a selective interfacial layer for the extraction of electrons or holes from OPVs.[27] Understanding how OSCs interact with graphene will be critical for further incorporation, and much work has been done on the graphene/OSC interface.[28–33] Recent work has shown how van der Waals epitaxy can result in the growth of large, highly crystalline OSC domains on graphene with improved device performance.[30,31] This epitaxial growth requires sufficient interaction between graphene and the molecule, and hence is limited to a subset of OSCs.

In this work, we present OMBD growth of VOPc onto chemical vapor deposition (CVD) grown graphene and investigate the effect of elevated substrate temperatures on the morphology and crystallinity of the OSC thin film. Atomic force microscopy (AFM) and X-ray diffraction (XRD) show that VOPc forms large grains on the graphene surface, which increase in size and crystallinity at higher temperatures. Low-dose aberration-corrected transmission electron microscopy (acTEM) shows that the large grains formed at elevated temperatures are single crystals of VOPc, with the molecules oriented perpendicular to the substrate. This alignment is in contrast to growth at ambient temperatures, where the film is composed of randomly orientated grains. At both ambient and elevated temperatures there is no epitaxial ordering relative to the graphene. Alongside this, deposition under similar conditions on substrates such as silicon oxide and graphene oxide (GO) results in much smaller OSC grain sizes. Finally, the mobility of the films is measured with conductive AFM (cAFM), with those deposited at elevated temperature displaying higher mobility and lower trapping. These observations highlight the impact elevated substrate temperatures during deposition have on the morphology and crystallinity of OSC thin films, and the potential importance of graphene for the deposition of high performance organic electronic devices.

2. Results and Discussion

2.1. Controlling VOPc Grain Size with Elevated Substrate Temperatures During Deposition

First we investigate the morphology of the VOPc films as a function of substrate temperate during deposition. In UHV, VOPc was sublimed from powder onto graphene on copper substrates at constant flux, with separate control of the substrate temperature. The deposition was monitored using a quartz crystal microbalance (QCM) to yield a 50 nm thick film at each temperature (see Section 1, Supporting Information, for effect of film thickness on deposition morphology).

Figure 1 shows AFM images of VOPc/Gr/Cu films deposited at different substrate temperatures but with otherwise identical experimental conditions. After deposition at 26 °C, the VOPc has formed a uniform grainy film. A measure of the grain size can be gained from analyzing the height–height correlation function of the AFM image; the correlation length provides an estimate of grain size (see Section 2, Supporting Information).[34] For the film deposited at room temperature (RT), the correlation length is (22 ± 3) nm. For 75 °C, a similar morphology is observed, but with a larger correlation length of (37 ± 3) nm, showing an increase in grain size. At 125 °C, the morphology changes and discrete islands are formed with areas of exposed substrate between them. At 155 °C, the islands increase in size and the surface coverage is reduced, a trend that continues at 175 °C.

From these morphological investigations, the grain sizes of the VOPc thin film can be quantified as a function of the substrate temperature. Percentage coverages and average island sizes for each deposition temperature are presented in Figure 1f. As the temperature increases, the typical island size increases from 10s of nanometers at room temperature to around a micrometer at 155 °C. Concomitant with this, the percentage of the surface covered by VOPc decreases from a continuous film at 26 and 75 °C, to only (21 ± 2)% coverage at 175 °C. In the higher temperature growth regime (with isolated islands), AFM investigations showed no evidence of a wetting layer; there is no VOPc on the graphene between the islands, indicating an island (Volmer–Weber) growth mode.

The morphological changes can be understood qualitatively by considering the growth dynamics.[35] After adsorbing, the molecules diffuse until they desorb, attach to an existing grain, or form a new nucleation site. On a homogeneous surface, the nucleation density is proportional to the deposition rate and inversely proportional to the diffusivity of the molecules on the surface.[36] If the deposition rate is constant, the nucleation density is determined by the diffusivity of molecules on the surface, which is typically governed by an Arrhenius factor and so is strongly dependent on temperature. At lower temperatures, diffusivity is low and the nucleation density is high, resulting in continuous thin films. As the substrate temperature increases, the diffusivity is higher and the nucleation rate is lower, resulting in larger islands. However, at even higher temperatures the rate of desorption becomes significant, hence the significantly decreased surface coverage at 175 °C.

As well as being dependent on growth temperature, the island size and nucleation density are dependent on the substrate–molecule interaction. For comparison, the morphology of VOPc deposited onto GO and silicon oxide was also investigated (see Sections 3 and 4, Supporting Information). GO is a heterogeneous material with a predominantly graphene-like lattice but decorated with oxygen containing functional groups such as epoxy and hydroxyl.[37] VOPc deposited at 155 °C showed increasing grain sizes from silicon oxide, to GO on silicon oxide, to free standing GO, but in all cases was significantly smaller than the island size on graphene on copper. The morphology of the VOPc growth on silicon oxide was similar to that reported previously.[23]

The comparison between suspended GO and GO supported on silicon oxide shows the importance of the underlying

DOI: 10.1002/adfm.201503594

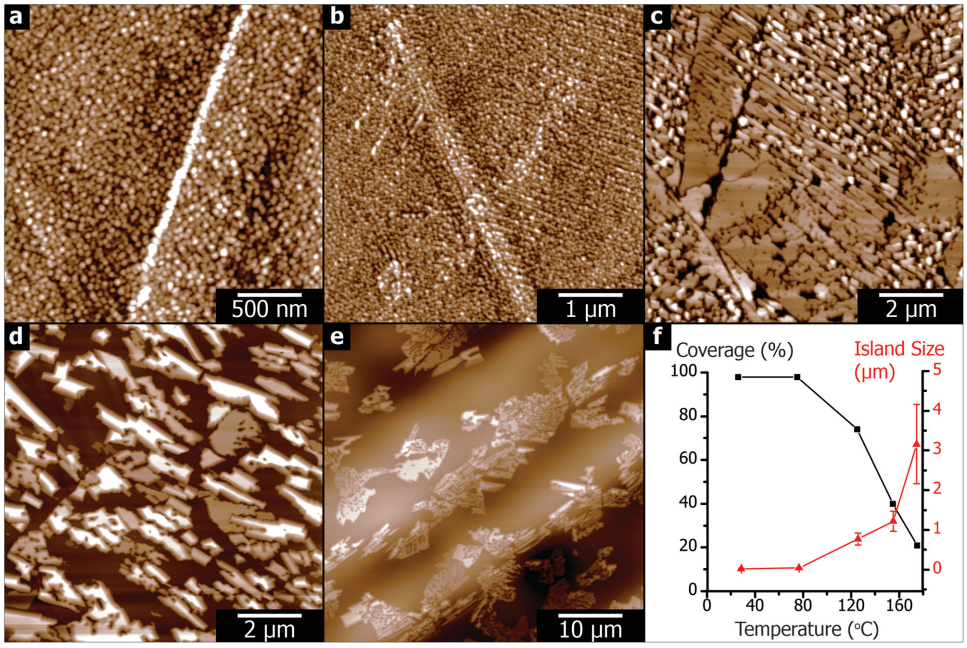

Figure 1. AFM showing morphology changes with increasing substrate temperature. At ambient temperature a) the film is grainy and rough, and b) is similar at 75 °C. c) At 125 °C substrate temperature discrete crystallites have formed with clear boundaries. At higher temperatures – d) 155 °C and e) 175 °C – the islands increase in size but reduce in number, causing a lower surface coverage. These changes are summarized in average island size and surface coverage statistics in (f). Full height scales are: a) 20 nm, b) 20 nm, c) 30 nm, d) 50 nm, and e) 800 nm.

substrate: graphene and GO films follow the substrate topography and rough substrates (like silicon oxide) cause strain and curvature in the film that increases the interaction with molecules. This reduces their diffusion rate and so increases the nucleation rate. On the other hand, graphene on copper is locally atomically flat, as shown in previous scanning tunneling microscopy (STM) investigations,[38] which aids the increase in OSC grain size. Inspection of the AFM images of the high temperature (HT) depositions in Figure 1 suggests that the VOPc island nucleation is, however, influenced by the topography of the Gr/Cu substrate, with islands tending to nucleate at regions of high curvature on the surface, but with no apparent effect from grain boundaries or wrinkles (see Section 5, Supporting Information, for AFM and scanning electron microscopy of the pristine Gr/Cu surface for comparison). This suggests that the VOPc grain size on graphene could be increased further by using a flatter substrate for the graphene, such as hexagonal boron nitride. Despite this, the VOPc island size seen here is still larger than that reported for VOPc deposited onto an order-inducing p-6P layer on silicon oxide.[21] This suggests that high quality OSC thin film deposition can be achieved on graphene without the need for order-inducing layers.

2.2. Effect of Substrate Temperature on Crystallinity of VOPc Thin Films

High-resolution XRD was used to determine the crystallographic changes with increasing substrate temperature, as shown in **Figure 2**. Peaks due to the polycrystalline copper are observed at every temperature and vary across samples. The low-cost copper foils that were used for graphene growth are polycrystalline and, although predominant crystallographic orientations are normally observed,[38,39] others are often present. For the sample deposited at 26 °C, there is a single peak in the diffraction pattern at $2\theta = (50.40 \pm 0.05)°$, indexed as the Cu(200) planes from the copper foil substrate, whilst on other samples a peak at $2\theta = (43.23 \pm 0.05)°$, assigned to Cu(111) planes, is also seen.

The XRD shows clear differences in the crystallography of VOPc with substrate temperature. At 26 °C no peaks are apparent that are attributable to VOPc. However, at 75 °C and higher, diffraction peaks corresponding to the VOPc crystal structure are apparent in the diffraction pattern. The single

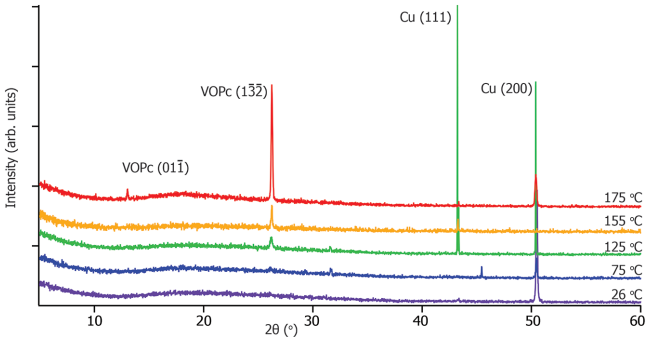

Figure 2. X-ray diffraction from films deposited on substrates at ambient and elevated temperatures. At ambient temperature (purple) only diffraction from the polycrystalline copper is seen. At higher temperatures, a peak at $2\theta = 27°$ appears and increases with increasing temperature. This peak is assigned to VOPc $(1\bar{3}2)$ planes. At the highest temperature (175 °C – red) diffraction from VOPc $(01\bar{1})$ planes appears.

peak at $2\theta = (26.23 \pm 0.05)°$, which increases in relative intensity with increasing substrate temperature, can be indexed to the $(1\bar{3}\bar{2})$ plane of VOPc. A previous study of VOPc deposited at elevated temperatures onto CuI also showed $(1\bar{3}\bar{2})$ planes in XRD measurements.[11] These planes correspond to the VOPc ligand-plane perpendicular to the surface, in an edge-on orientation. This geometry is in contrast to previous reports on the planar MPc CuPc, which has been shown to stack face-on on graphene.[15]

Thus XRD shows that the crystallinity increases with increasing substrate temperature and determines the macroscopically averaged orientation of the VOPc relative to the substrate surface.

2.3. Determination of Molecular Crystallography

The nanoscale crystallography of the VOPc grains was investigated by low-dose TEM diffraction and acTEM imaging. Prior work has shown that TEM is an effective method for investigating the nanoscale heterogeneity of molecular thin films. For example, scanning TEM has been used to study grain boundaries in molecular crystals[40] and high-resolution TEM (HRTEM) to study the molecular interface of a CuPc/C60 active layer in an OPV.[41] CVD graphene provides the ideal TEM support to study molecular layers because it contributes virtually no contrast to images. Additionally, the organic molecules can be directly deposited onto graphene (as recently shown for the deposition of C_{60}[42] and pentacene[43]), which removes any degradation of the film during the transfer process, or during focused ion beam lift-out preparation.[44] Here VOPc was deposited directly onto graphene coated TEM supports (see the Experimental Section for details).

Electron diffraction from discrete islands shows that they are composed of one crystalline domain and resolves their orientation relative to graphene. TEM analysis of VOPc deposited at 155 °C on a graphene coated grid is shown in **Figure 3**, with further low magnification images in Section 6 of the Supporting Information. The VOPc island morphology on the free-standing graphene is similar to that on graphene on copper. However, the island sizes are smaller due to the effects of the residue from the transfer process (see Section 7, Supporting Information), which is known to influence the growth of OSC structures on graphene.[32] Figure 3b shows a low-dose (see Section 8, Supporting Information, for details of low-dose procedures), selected-area electron diffraction pattern from the island highlighted in white in Figure 3a. The pattern shows sharp diffraction spots that are indicative of crystalline VOPc and are consistent with the molecules being ordered close to the $[1\bar{3}\bar{2}]$ direction relative to the graphene surface, as previously suggested by the XRD measurements. Molecular models of this orientation are given in Figure 3d,e. A simulated diffraction pattern from this proposed structure is shown in Figure 3c. The spots closest to the direct beam are the (110) and $(\bar{1}\bar{1}0)$ planes as marked; these match well in position and magnitude to the experimental diffraction pattern. The electron diffraction pattern is thus from a single orientation of VOPc indicating that the island is a single crystal.

The crystallographic orientation of the underlying graphene can be found by electron diffraction after longer exposures (see Section 9, Supporting Information). Analysis of many VOPc islands showed no preferential orientations between the VOPc and graphene. This indicates that there is no epitaxial relation here between VOPc and graphene: the VOPc molecules are "standing up" relative to the graphene surface but each crystalline island is randomly orientated within that plane.

Further insight into the crystallographic arrangement within the islands can be gained from high resolution imaging. **Figure 4** shows low-dose acTEM of VOPc deposited on graphene at 155 °C. The high resolution images resolve the lattice planes, as in Figure 4 which shows a region at the interface between two islands of different in-plane orientation. Fast

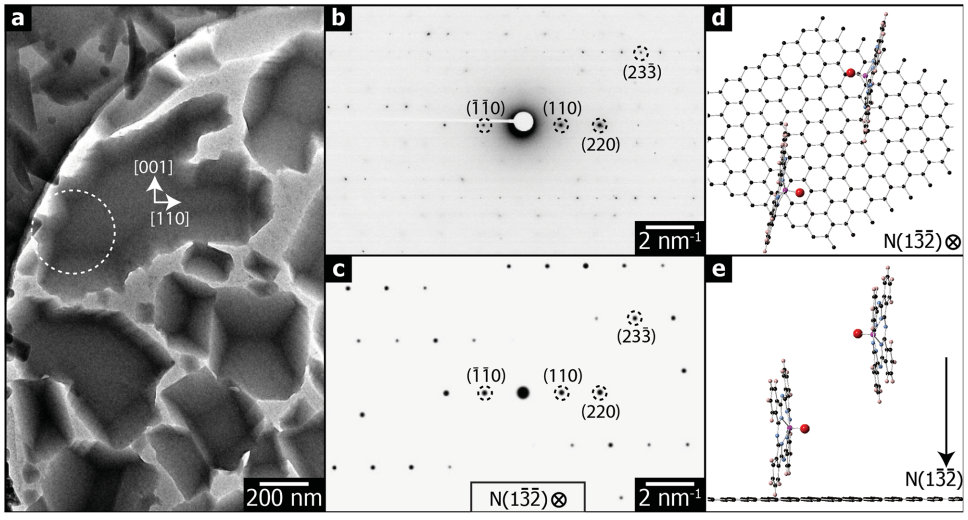

Figure 3. TEM of VOPc deposited at 155 °C onto graphene on a TEM grid. a) A low-magnification image that shows darker contrast features on graphene with a similar morphology to that seen when VOPc is deposited onto graphene on copper. b) A diffraction pattern from the region indicated with the white circle in (a). This pattern is consistent with the electron beam normal to the VOPc $(1\bar{3}\bar{2})$ planes, with a predicted pattern shown in (c). The crystal structure of this arrangement is shown in (d) and (e), and these VOPc crystal directions are shown on the image in (a).

DOI: 10.1002/adfm.201503594

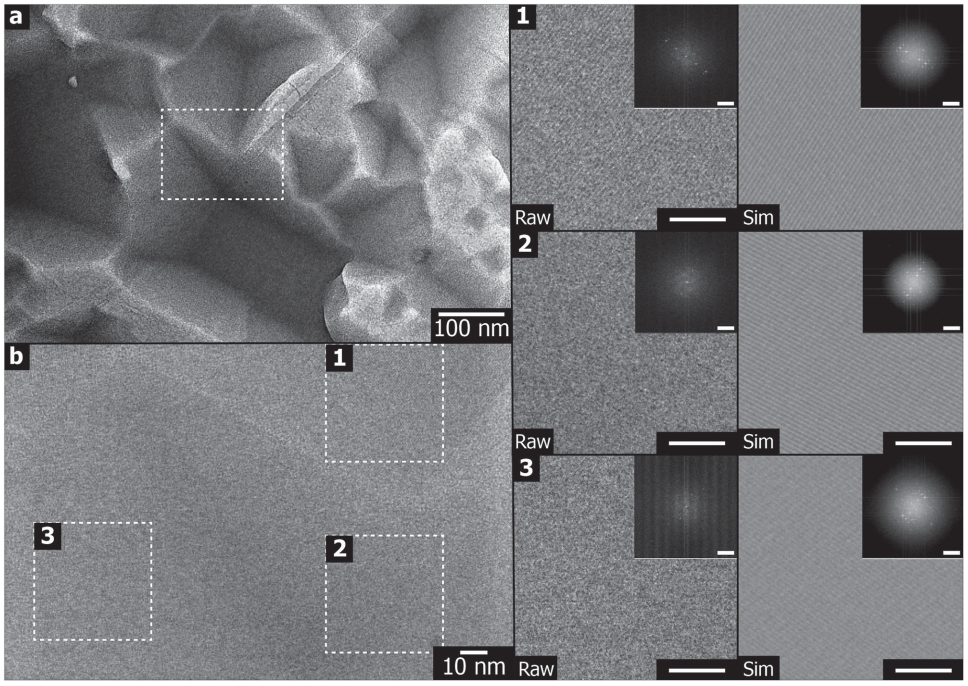

Figure 4. acTEM of VOPc deposited onto a graphene coated TEM grid at 155 °C. a) A low magnification image. b) A higher magnification image of the region marked in (a). Sections of this image are highlighted in the right panels, with FFTs inset. Next to these are multislice simulations the expected crystal structure, again with their FFTs inset. In these panels, image scale bars are 10 nm and FFT scale bars are 2 nm^{-1}.

Fourier transforms (FFTs) from regions within each island show distinct spots, which in Figure 4b, areas 1 and 2, correspond to lattice spacings consistent with the (110) and $(\overline{1}\overline{1}0)$ planes as expected from the electron diffraction pattern, and demonstrate the change of orientation between islands. Multislice TEM image simulations, with molecular orientations as for the simulated diffraction pattern in Figure 3, are also shown in Figure 4 and again match well with the experimental images. The lattice resolution images in areas 1 and 2 are from near the edge of the islands, as marked. In the region closer to the center of the island, area 3, the FFT shows spots from (110) planes and further spots that can be identified as from (221) planes of VOPc. These arise from molecules stood up on the graphene surface but that are tilted by 2° from the $[1\overline{3}2]$ direction. Molecules oriented in this way are only seen near the center of the crystalline island and could be indicative of a small amount of strain within the islands due to thermal stress on cooling, although we cannot rule out imaging artifacts caused by the early stages of electron beam damage.

TEM analysis of VOPc films deposited at room temperature shows a very different nanoscale crystallography to the single crystal islands at high temperature. The granular film morphology shown in the bright field TEM image in **Figure 5** is consistent with that observed in AFM, with grain sizes of order 10s of nm across. Figure 5b shows a low dose selected area electron diffraction pattern from the area circled in white: the hexagonal spots due to the underlying graphene can be resolved as well as rings due to VOPc. The rings indicate again no epitaxial alignment relative to the graphene. High resolution images, Figure 5c, confirm that although the grains are small they are still crystalline. However, the grain size is smaller than the film thickness so it is not easily possible from the electron diffraction or HRTEM data to determine the orientation of the VOPc at the graphene surface.

2.4. Correlating Crystallinity and Mobility

The charge carrier mobility is a key parameter for OSC device performance. Conductive AFM (cAFM) was used to probe the mobility through VOPc films on graphene on copper in order to correlate structural changes with changes in transport properties. In cAFM the current flow between a conductive AFM tip and sample surface is measured. For OSC thin films, the mobility can be determined by acquiring current–voltage (i–V) curves at fixed positions on a sample. At high bias voltages the transport is dominated by space charge limited current. Correcting for the nonplanar geometry in the case of cAFM, Reid et al. proposed a modified Mott–Gurney equation to describe this[45]

$$J = \alpha\delta_J \varepsilon_0 \varepsilon_r \mu_0 e^{\left(0.89\gamma\sqrt{V/L}\right)} \frac{V^2}{L^3}\left(\frac{L}{2r_c}\right)^{1.6} \quad (1)$$

where J is the current density at the tip (i.e., current divided by the tip surface contact area), ε_0 and ε_r are the vacuum permittivity and the relative permittivity of the thin film, respectively, μ_0 is the zero field mobility, and L is the thickness of the OSC thin film. α is a prefactor determined by Reid et al. from finite element modeling to account for the nonuniform electrical field (α = 8.2 in place of 9/8 for the Mott–Gurney law for planar electrodes). The factor $e^{\left(0.89\gamma\sqrt{V/L}\right)}$ accounts for

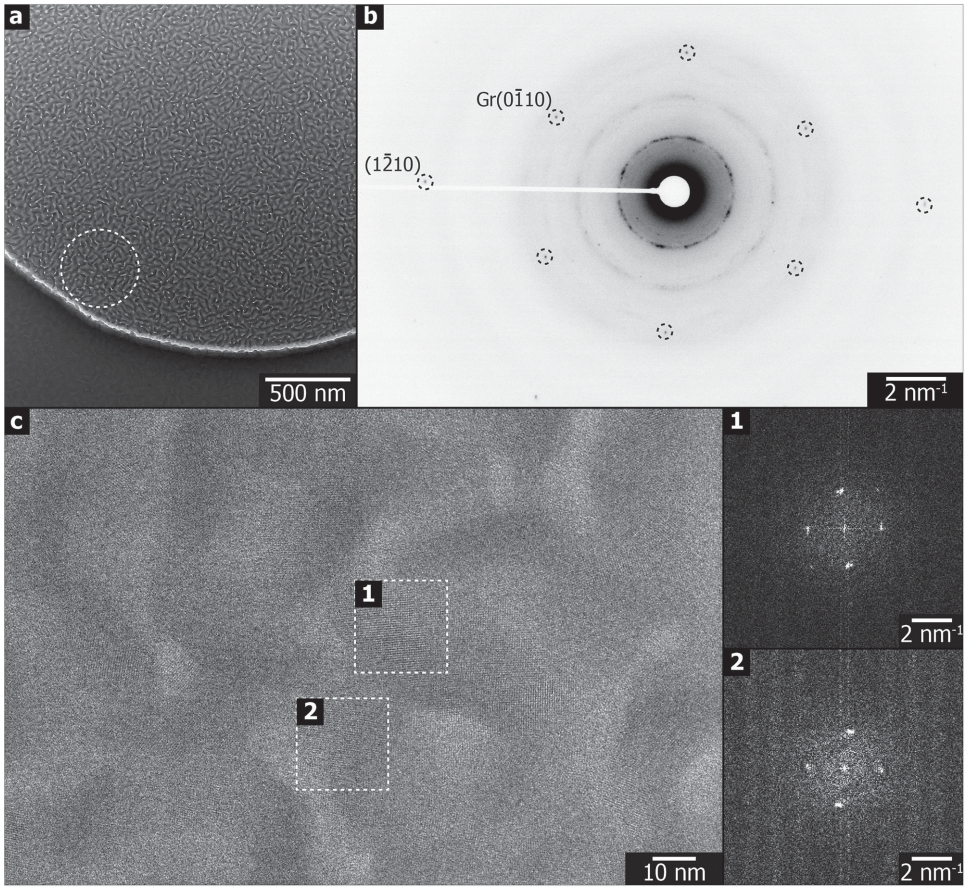

Figure 5. TEM of a VOPc film deposited onto graphene at 26 °C. a) A low-magnification image of a VOPc coated region. The film morphology is similar to that observed in AFM measurements. b) A diffraction pattern from the region marked in (a). The graphene spots are labeled. Also present are rings indicating a polycrystalline VOPc film. c) High magnification image, with FFTs of the marked regions. These show that within the film there are crystalline domains around 10 nm across.

the electric field dependence of the mobility, where γ quantifies the strength of the field dependence and has been related to trapping within the OSC: higher values of γ are interpreted as indicative of more charge trapping within the film. The constant δ_J was included by Reid et al. to empirically account for the difference between mobilities from cAFM measurements and those from planar electrodes. A key parameter is the contact radius, r_c, between the tip and sample. A more accurate value for this can be determined by modeling the tip-sample contact according to the Johnson–Kendall–Roberts model.[46] Taking into account the correct contact radius, our prior work showed that the empirical factor δ_J is not required and so here is set to 1.[47] Fitting the current–voltage curves to Equation (1) thus gives values for the mobility and γ.

A typical cAFM i–V curve from the VOPc on graphene on copper is shown in **Figure 6**a (with more i–V curves presented in Section 10, Supporting Information), along with the fit to Equation (1) (red line). The curve is asymmetric due to the difference in contacts: the top contact is the Pt AFM tip (work function 6.4 eV),[48] whilst the bottom contact is the graphene on copper (work function 4.6 eV).[49] Here the bias is applied to the sample (i.e., back-electrode) with the tip at virtual earth. Measurements were made across several areas on both high temperature (130 °C) deposited VOPc on graphene on copper (HT samples) and room temperature deposited VOPc on graphene on copper (RT samples). The sample morphologies were as in Figure 1. The results are summarized in Figure 6b which shows a scatter plot of mobility versus γ, with results on HT samples in red and RT samples in blue. The average value of the mobility is roughly twice as high for the HT compared to the RT (0.27 ± 0.04 cm^2 V^{-1} s^{-1} for HT and 0.14 ± 0.08 cm^2 V^{-1} s^{-1} for RT) and is consistent with prior reports of high mobility in VOPc.[21,23] The average value of γ decreases from $(-1.2 \pm 0.2) \times 10^{-4}$ m$^{1/2}$ V$^{-1/2}$ for RT to $(-1.7 \pm 0.1) \times 10^{-4}$ m$^{1/2}$ V$^{-1/2}$ for the high temperature deposition, which suggests a decrease in trapping for the HT sample. The comparatively high mobility value for the HT sample is despite the VOPc being "stood up" relative to the graphene which should increase charge transport laterally through the film (as in a OTFT measurement) rather than vertically through it as probed here.

The scatter plot in Figure 6b demonstrates other clear differences between the samples. Values of mobility and γ for the HT sample are fairly consistent and uncorrelated, indicating homogeneous conductivity on the VOPc islands. By contrast, the RT sample shows a wide range of mobilities and γ, with a clear correlation between them such that the higher mobilities are

DOI: 10.1002/adfm.201503594

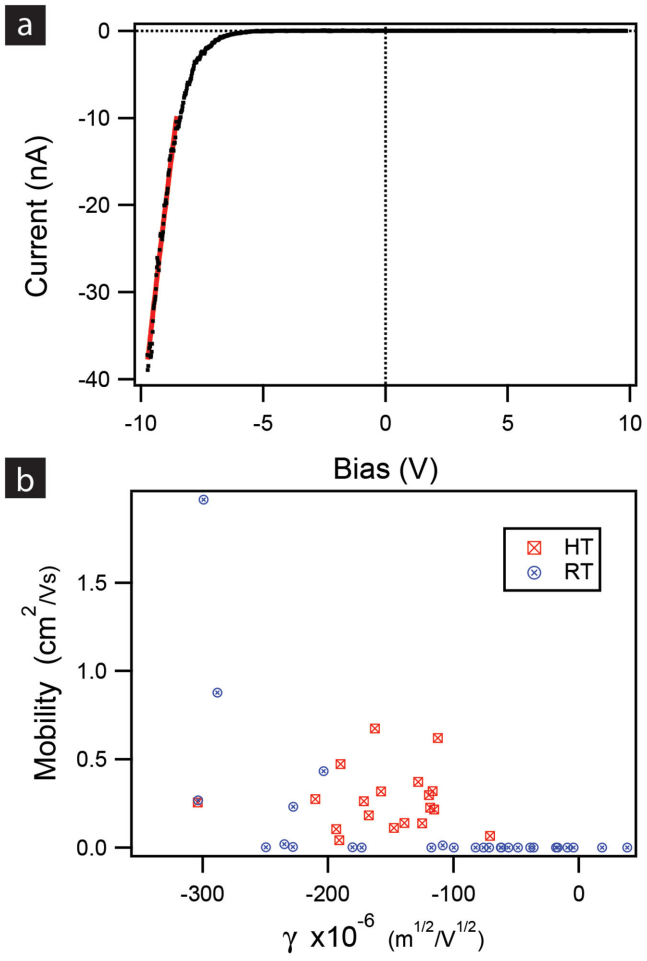

Figure 6. cAFM of VOPc films deposited at RT (26 °C) and HT (155 °C). a) Current–voltage curve acquired on a high temperature sample (black points), the high negative bias region is fit (red line) by a modified Mott–Gurney equation as described in the main text. b) Scatter plot of the zero field mobility plotted against the field dependence of the mobility, γ, with measurements taken on high temperature deposited samples shown in red and room temperature deposited samples shown in blue.

correlated to lower γ. This heterogeneous response is consistent with the small grain size in the room temperature deposited films: at the nanoscale the conductivity depends on the local orientation of the VOPc grains and the number of grain boundaries between tip and graphene back contact at that point.

3. Conclusion

In summary, we have found that single crystals of VOPc several micrometers across can be grown on CVD-grown graphene using elevated substrate temperatures of 155 °C. This is in contrast to deposition on graphene at ambient temperatures, where VOPc grains grow to only tens of nanometers across. Further, these large grains form only on the homogeneous graphene surface; on the heterogeneous surfaces of graphene oxide and silicon oxide, grain sizes are an order of magnitude smaller. No epitaxial relationship is observed between the deposited VOPc molecules and the graphene, so the increase in grain size is not directly linked to van der Waals epitaxy. However, the van der Waals nature does encourage high diffusion rates that promote ordered OSC films. To capitalize on this, it will be important to utilize clean graphene and to minimize the roughness of the underlying substrate. van der Waals epitaxy of OSCs on graphene can only be achieved for a limited subset of molecules, but the results presented here show that the weak interaction between graphene and molecules should promote the formation of more ordered OSC films without the need for order-inducing layers.

4. Experimental Section

Graphene Growth: Graphene was grown on low cost copper foils via low pressure CVD using methane as a feedstock.[50] First, the copper foils were electropolished[51] in a solution containing orthophosphoric acid and urea (5 V, 1.5 A). After rinsing off the electrolyte with deionized water then isopropanol, the polished foils were sonicated in acetone, and then rinsed again with isopropanol and dried with nitrogen. They were loaded into a quartz tube in a tube furnace, which was pumped to vacuum below 1×10^{-3} mbar. Hydrogen was flowed at 10 standard cubic centimeters per minute (sccm), raising the pressure to 1×10^{-2} mbar. The furnace was heated to 1000 °C, and left to anneal for 20 min. This yields copper foils that are >99% covered with predominantly single layer graphene of high-quality[38] (see the Supporting Information for AFM of pristine graphene).

Graphene Transfer: To transfer graphene to TEM grids, the graphene-coated foils were first spin-coated with formvar (3.4 mg mL^{-1}) using spin speed 3000 rpm, ramp 0.1 s, and dwell 45 s. The coated foils were then placed into ammonia persulphate to etch away the copper overnight. Once the copper was removed, the foils were transferred to deionized water, repeating this to fresh water five times to remove any remaining etchant. The floating stack was then scooped using SiN TEM supports (from Silson) and left to dry in air. The grids were then placed in chloroform for 10 min to remove the formvar. They were then transferred to acetone, and then to a critical point dryer, to dry without surface tension breaking the films. Finally, the TEM grids were further cleaned by heating on a hotplate at 200 °C for 2 h.

Graphene Oxide Sample Preparation: Graphene oxide paper was produced via a modified Hummer's method as reported previously.[37] The paper was then dissolved in deionized water. For GO on silicon oxide, the solution was diluted to 2 mg mL^{-1}. A silicon oxide substrate was plasma cleaned (1 min, 100 W) and the graphene oxide deposited by spin coating (0.1 s ramp, 3000 rpm, 45 s dwell). For GO on TEM supports, the solution was diluted to 0.01 mg mL^{-1}. A lacy carbon TEM support (EM Resolutions, product code LC400Cu) was plasma cleaned (1 min, 100 W) and then a single drop of GO solution was cast onto the grid and left in air to dry. The substrates were then transferred to UHV for VOPc deposition.

VOPc Deposition: Vanadyl phthalocyanine (VOPc) was deposited directly onto graphene coated foils, or onto graphene coated SiN grids, in a custom-built single chamber UHV system with a base pressure better than 1×10^{-8} mbar. VOPc (Acros Organics UK) was purified by three cycles of thermal gradient sublimation before use. All films were grown at a deposition rate (monitored by a QCM) of 0.03 nm s^{-1} which corresponded to a crucible temperature of ≈365 °C. The substrate temperatures used for growth are indicated in the text. The graphene covered foils or TEM grids were heated to the target temperature and left for one hour to reach equilibrium, during which time the VOPc deposition rate was stabilized. Once deposition was complete, the foils or grids were left to cool and removed from UHV to be examined.

X-Ray Diffraction: Thin film XRD patterns were obtained using a Panalytical X'Pert Pro MRD diffractometer with monochromatic Cu Kα1 radiation.

Aberration-Corrected TEM: For acTEM, a JEOL ARM 200F was used, operating at 80 kV, with CEOS probe and image aberration correction. The dose was estimated by measuring the current draining to earth from the phosphor screen when illuminated by the electron beam. This was then adjusted to 100 e^{-} $Å^{-2}$ s^{-1} for high magnification imaging and to 5 e^{-} $Å^{-2}$ s^{-1} for diffraction.

TEM Simulations: Diffraction patterns were simulated with Single Crystal Diffract software for Crystal Maker. High-resolution images were simulated using a custom-made multislice procedure.[52]

AFM and cAFM: An Asylum Research MFP3D-SA was used for AFM and cAFM measurements. AFM images were taken in ac-mode. The cAFM measurements used the Asylum Research ORCA current preamplifier and followed the experimental method described in detail in Wood et al.[47] In brief, current–voltage curves were acquired with the tip held stationary on the sample at set and constant contact force, simultaneously to the acquisition of force–distance curves. This was repeated on a grid, in a manner analogous to a force–volume measurement. Comparison with topography images acquired before this acquisition showed minimal sample drift. For the HT sample, this procedure was followed on small regions of individual islands, with their heights measured by larger topography images. For the RT sample, the film thickness was measured by imaging across a scratch through the film. Pt tips (Rocky Mountain Nanotechnology 25PT300B probes, with cantilevers of nominal resonance frequency 20 kHz, spring constant 18 N m^{-1}, and tips of nominal radius 10 nm) were used for the cAFM measurements. The Young's modulus of the VOPc was measured independently by analysis of force curves using Vecco Multi130PT cantilevers (spring constant 6.49 N m^{-1}), giving a value of (2.0 ± 0.3) GPa, which was used in the contact area calculations. Cantilevers were calibrated using the Sader method.[53] Typical contact areas were 100–1000 nm^2 (determined for each current–voltage measurement by fitting the relevant force curves) along with applied forces of 20–50 nN (measured for each current–voltage measurement by fitting the relevant force curves).

Supporting Information

Supporting Information is available from the Wiley Online Library or from the author.

Acknowledgements

A.J.M. and L.R. contributed equally to this work. The Engineering and Physical Sciences Research Council (EPSRC), UK, is thanked for support through studentships for A.J.M. and D.W. (EP/K503204/1), for A.J.R. through EP/G037515/1, for L.R. and T.S.J. through EP/H021388/1, and for funding for open access charges. Oxford Instruments Asylum Research is thanked for their support of D.W. The Panalytical MRD diffractometer used in this research was obtained through the Science City Advanced Materials Project: Creating and Characterizing Next Generation Advanced Materials, with support from Advantage West Midlands (AWM) and part funded by the European Regional Development Fund (ERDF). All data created for this publication are openly available from http://doi.org/10.17632/mcrbjymjp5.1.

Received: August 25, 2015
Revised: October 28, 2015
Published online:

[1] P. M. Beaujuge, J. M. J. Fréchet, *J. Am. Chem. Soc.* **2011**, *133*, 20009.
[2] M. Mas-Torrent, C. Rovira, *Chem. Rev.* **2011**, *111*, 4833.
[3] C. Wang, H. Dong, W. Hu, Y. Liu, D. Zhu, *Chem. Rev.* **2012**, *112*, 2208.
[4] S. Günes, H. Neugebauer, N. S. Sariciftci, *Chem. Rev.* **2007**, *107*, 1324.
[5] A. J. Heeger, *Chem. Soc. Rev.* **2010**, *39*, 2354.
[6] M. G. Walter, A. B. Rudine, C. C. Wamser, *J. Porphyrins Phthalocyanines* **2010**, *14*, 759.
[7] B. P. Rand, D. Cheyns, K. Vasseur, N. C. Giebink, S. Mothy, Y. Yi, V. Coropceanu, D. Beljonne, J. Cornil, J.-L. Brédas, J. Genoe, *Adv. Funct. Mater.* **2012**, *22*, 2987.
[8] R. S. Sposili, J. S. Im, *Appl. Phys. Lett.* **1996**, *69*, 2864.
[9] J. Rivnay, L. H. Jimison, J. E. Northrup, M. F. Toney, R. Noriega, S. Lu, T. J. Marks, A. Facchetti, A. Salleo, *Nat. Mater.* **2009**, *8*, 952.
[10] S. Kowarik, A. Gerlach, F. Schreiber, *J. Phys. Condens. Matter* **2008**, *20*, 184005.
[11] A. J. Ramadan, L. A. Rochford, D. S. Keeble, P. Sullivan, M. P. Ryan, T. S. Jones, S. Heutz, *J. Mater. Chem. C* **2015**, *3*, 461.
[12] L. Li, Q. Tang, H. Li, W. Hu, *J. Phys. Chem. B* **2008**, *112*, 10405.
[13] G. de la Torre, C. G. Claessens, T. Torres, *Chem. Commun.* **2007**, 2000.
[14] S. Pfuetzner, J. Meiss, A. Petrich, M. Riede, K. Leo, *Appl. Phys. Lett.* **2009**, *94*, 2007.
[15] J. M. Mativetsky, H. Wang, S. S. Lee, L. Whittaker-Brooks, Y.-L. Loo, *Chem. Commun.* **2014**, *50*, 5319.
[16] H. G. Zhang, J. T. Sun, T. Low, L. Z. Zhang, Y. Pan, Q. Liu, J. H. Mao, H. T. Zhou, H. M. Guo, S. X. Du, F. Guinea, H.-J. Gao, *Phys. Rev. B* **2011**, *84*, 245436.
[17] S. J. Altenburg, M. Lattelais, B. Wang, M.-L. Bocquet, R. Berndt, *J. Am. Chem. Soc.* **2015**, *137*, 9452.
[18] H. Y. Mao, R. Wang, Y. Wang, T. C. Niu, J. Q. Zhong, M. Y. Huang, D. C. Qi, K. P. Loh, A. T. S. Wee, W. Chen, *Appl. Phys. Lett.* **2011**, *99*, 093301.
[19] B. Verreet, R. Müller, B. P. Rand, K. Vasseur, P. Heremans, *Org. Electron.* **2011**, *12*, 2131.
[20] F. Pan, H. Tian, X. Qian, L. Huang, Y. Geng, D. Yan, *Org. Electron.* **2011**, *12*, 1358.
[21] H. Wang, D. Song, J. Yang, B. Yu, Y. Geng, D. Yan, *Appl. Phys. Lett.* **2007**, *90*, 253510.
[22] J. Yang, D. Yan, *Chem. Soc. Rev.* **2009**, *38*, 2634.
[23] X. J. Yu, J. B. Xu, W. Y. Cheung, N. Ke, *J. Appl. Phys.* **2007**, *102*, 103711.
[24] A. C. Ferrari, F. Bonaccorso, V. Fal'ko, K. S. Novoselov, S. Roche, P. Bøggild, S. Borini, F. H. L. Koppens, V. Palermo, N. Pugno, J. A. Garrido, R. Sordan, A. Bianco, L. Ballerini, M. Prato, E. Lidorikis, J. Kivioja, C. Marinelli, T. Ryhänen, A. Morpurgo, J. N. Coleman, V. Nicolosi, L. Colombo, A. Fert, M. Garcia-Hernandez, A. Bachtold, G. F. Schneider, F. Guinea, C. Dekker, M. Barbone, Z. Sun, C. Galiotis, A. N. Grigorenko, G. Konstantatos, A. Kis, M. Katsnelson, L. Vandersypen, A. Loiseau, V. Morandi, D. Neumaier, E. Treossi, V. Pellegrini, M. Polini, A. Tredicucci, G. M. Williams, B. Hee Hong, J.-H. Ahn, J. Min Kim, H. Zirath, B. J. van Wees, H. van der Zant, L. Occhipinti, A. Di Matteo, I. A. Kinloch, T. Seyller, E. Quesnel, X. Feng, K. Teo, N. Rupesinghe, P. Hakonen, S. R. T. Neil, Q. Tannock, T. Löfwander, J. Kinaret, *Nanoscale* **2015**, *7*, 4598.
[25] H. Park, P. R. Brown, V. Bulović, J. Kong, *Nano Lett.* **2012**, *12*, 133.
[26] T.-B. Song, N. Li, *Electronics* **2014**, *3*, 190.
[27] D. W. Chang, H.-J. Choi, A. Filer, J.-B. Baek, *J. Mater. Chem. A* **2014**, *2*, 12136.
[28] G. Hlawacek, F. S. Khokhar, R. Van Gastel, B. Poelsema, C. Teichert, *Nano Lett.* **2011**, *11*, 333.
[29] G. Hong, Q.-H. Wu, J. Ren, C. Wang, W. Zhang, S.-T. Lee, *Nano Today* **2013**, *8*, 388.
[30] C.-H. Lee, T. Schiros, E. J. G. Santos, B. Kim, K. G. Yager, S. J. Kang, S. Lee, J. Yu, K. Watanabe, T. Taniguchi, J. Hone, E. Kaxiras, C. Nuckolls, P. Kim, *Adv. Mater.* **2014**, *26*, 2812.
[31] D. He, Y. Zhang, Q. Wu, R. Xu, H. Nan, J. Liu, J. Yao, Z. Wang, S. Yuan, Y. Li, Y. Shi, J. Wang, Z. Ni, L. He, F. Miao, F. Song, H. Xu, K. Watanabe, T. Taniguchi, J. Xu, X. Wang, *Nat. Commun.* **2014**, *5*, 1.

[32] M. Kratzer, B. C. Bayer, P. R. Kidambi, A. Matković, R. Gajić, A. Cabrero-Vilatela, R. S. Weatherup, S. Hofmann, C. Teichert, *Appl. Phys. Lett.* **2015**, *106*, 103101.
[33] G.-H. Lee, C.-H. Lee, A. M. van der Zande, M. Han, X. Cui, G. Arefe, C. Nuckolls, T. F. Heinz, J. Hone, P. Kim, *APL Mater.* **2014**, *2*, 092511.
[34] T. Gredig, E. A. Silverstein, M. P. Byrne, *J. Phys. Conf. Ser.* **2013**, *417*, 012069.
[35] J. A. Venables, G. D. T. Spiller, M. Hanbucken, *Rep. Prog. Phys.* **1984**, *47*, 399.
[36] N. N. Nguyen, S. B. Jo, S. K. Lee, D. H. Sin, B. Kang, H. H. Kim, H. Lee, K. Cho, *Nano Lett.* **2015**, *15*, 2474.
[37] N. R. Wilson, P. A. Pandey, R. Beanland, R. J. Young, I. A. Kinloch, L. Gong, Z. Liu, K. Suenaga, J. P. Rourke, S. J. York, J. Sloan, *ACS Nano* **2009**, *3*, 2547.
[38] N. R. Wilson, A. J. Marsden, M. Saghir, C. J. Bromley, R. Schaub, G. Costantini, T. W. White, C. Partridge, A. Barinov, P. Dudin, A. M. Sanchez, J. J. Mudd, M. Walker, G. R. Bell, *Nano Res.* **2013**, *6*, 99.
[39] J. D. Wood, S. W. Schmucker, A. S. Lyons, E. Pop, J. W. Lyding, *Nano Lett.* **2011**, *11*, 4547.
[40] M. Haruta, H. Kurata, *Sci. Rep.* **2012**, *2*, 2.
[41] J. B. Gilchrist, T. H. Basey-Fisher, S. C. Chang, F. Scheltens, D. W. McComb, S. Heutz, *Adv. Funct. Mater.* **2014**, *24*, 6473.
[42] K. Kim, T. H. Lee, E. J. G. Santos, P. S. Jo, A. Salleo, Y. Nishi, Z. Bao, *ACS Nano* **2015**, *9*, 5922.
[43] K. Kim, E. J. G. Santos, T. H. Lee, Y. Nishi, Z. Bao, *Small* **2015**, *11*, 2037.
[44] E. Montoya, S. Bals, M. D. Rossell, D. Schryvers, G. Van Tendeloo, *Microsc. Res. Tech.* **2007**, *70*, 1060.
[45] O. G. Reid, K. Munechika, D. S. Ginger, *Nano Lett.* **2008**, *8*, 1602.
[46] H.-J. Butt, B. Cappella, M. Kappl, *Surf. Sci. Rep.* **2005**, *59*, 1.
[47] D. Wood, I. Hancox, T. S. Jones, N. R. Wilson, *J. Phys. Chem. C* **2015**, *119*, 11459.
[48] P. A. Tipler, R. A. Llewellyn, *Modern Physics*, 3rd ed., W. H. Freeman, New York **1999**.
[49] Y.-J. Yu, Y. Zhao, S. Ryu, L. E. Brus, K. S. Kim, P. Kim, *Nano Lett.* **2009**, *9*, 3430.
[50] X. Li, W. Cai, J. An, S. Kim, J. Nah, D. Yang, R. Piner, A. Velamakanni, I. Jung, E. Tutuc, S. K. Banerjee, L. Colombo, R. S. Ruoff, *Science* **2009**, *324*, 1312.
[51] B. Zhang, W. H. Lee, R. Piner, I. Kholmanov, Y. Wu, H. Li, H. Ji, R. S. Ruoff, *ACS Nano* **2012**, *6*, 2471.
[52] M. A. Dyson, *Ph.D. Thesis*, University of Warwick, **2015**.
[53] J. E. Sader, J. W. M. Chon, P. Mulvaney, *Rev. Sci. Instrum.* **1999**, *70*, 3967.